

Stabilization of higher-order vortex solitons by means of nonlocal nonlinearityHuicong Zhang ^{*}, Tao Zhou, and Chaoqing Dai[†]*College of Optical, Mechanical and Electrical Engineering, Zhejiang A&F University, Hangzhou 311300, China*

(Received 28 October 2021; accepted 7 January 2022; published 20 January 2022)

We report the experimental observation of the instability suppression of higher-order vortex solitons in cylindrical lead glass with thermal nonlocal nonlinearity. A scalar higher-order vortex soliton with a topological charge $l = 10$, which is vulnerable to azimuthal breakup when it is perturbed by an initial noise, is stabilized by a coaxially propagating, mutually incoherent Gaussian beam, forming a Gauss-vortex vector soliton (GVVS). The vortical annular profile and topological charge in the GVVS, and the vortical annular profile in the Gauss-vortex vector breather (GVVB), can be preserved during the propagation. Numerical simulations for unperturbed and perturbed scalar vortex solitons, GVVS, and GVVB demonstrate close agreement with experimental results.

DOI: [10.1103/PhysRevA.105.013520](https://doi.org/10.1103/PhysRevA.105.013520)**I. INTRODUCTION**

Light beams carrying orbital angular momentum (OAM) are usually associated with optical vortices, which feature a hollow core surrounded by a toroid-shaped intensity profile. Due to their fascinating properties, including the screw-type wave front [1], energy flow within a cross section [2], and unlimited value of topological charge [3], optical vortices possess considerable promise for applications in information encoding and processing [4], OAM multiplexing [5,6], and rotating Doppler effect [7], among others. When a vortex beam propagates in a nonlinear medium, the combined effect between self-focusing and diffraction may lead to its non-diffracting propagation, forming a spatial vortex soliton. Two-dimensional (2D) solitons with embedded vorticities have garnered growing interest because of their concentration of energy in space and power handling capabilities [8,9]. However, a well-known problem impeding the application of vortex solitons in self-focusing nonlinear media is vortex breakup driven by the intrinsic azimuthal instability [10]; this process has been observed experimentally in nematic liquid crystals (NLCs) [11], saturable vapors [12], and photorefractive nonlinear media [13].

Many physically relevant settings and models were proposed to prevent the breakup of bright vortex soliton with topological charge $l = 1$. The stable scalar (single-component), single-charged vortex soliton was theoretically proposed in cubic self-focusing and quintic self-defocusing nonlinear media [14] and Bose-Einstein condensates (BECs) [15], and experimentally observed in square lead glass [16] and bulk NLC [17], both of which feature strongly nonlocal nonlinearity. A self-confined scalar vortex nematicon was recently achieved in planar NLC cells, with the aid of material nonlocality and low birefringence [18]. Another route towards vortex-annulus stabilization relied on the vector (multicom-

ponent) vortex solitons (VVVs). A class of two-color VVs, denoted by the $(0, 1)$ state, was predicted in theory [19,20] and implemented in NLC experiments [21,22]. It revealed that the crater-shaped vortex can be confined by the nonlocal refractive potential induced by the bell-shaped fundamental beam. Another class of two-component VVs, denoted by the $(+1, -1)$ state, shows that the vortex pair with hidden vorticity always exhibits better stability than one with explicit vorticity in NLCs [23,24], as well as BECs with attractive interactions [25].

Motivated by applications in such areas as multichannel communication [26] and yeast cell trapping [27], the stabilization of the vortex soliton with a large value of topological charge has become an especially interesting research topic. Vortex solitons with $l > 2$ may be stable in media with quadratic-cubic [28], and cubic-quintic nonlinearities [29]. Li *et al.* constructed 2D self-trapped vortical quantum droplets, and found the quantum droplets with charge up to 5 are stable within a certain norm region [30]. Another possibility to create stable 2D giant vortex rings (vortex solitons with an indefinitely large value of charges) was predicted in binary BEC with its two components coupled by microwave radiation [31,32]. With respect to the higher-order vortices in coupling systems, we theoretically discovered that the azimuthal instability of a higher-order ($l > 2$) vortex can be eliminated by a lower-order ($l \leq 2$) vortex, including the fundamental beam, in thermal nonlocal media with cylindrical symmetry, even when the higher-order charge is extremely large [33,34].

In this work, we experimentally demonstrate the formation of a Gauss-vortex vector soliton (GVVS) and a Gauss-vortex vector breather (GVVB), both of which consist of one higher-order ($l = 10$) bright vortex being stabilized by the other fundamental Gaussian beam, in one of the most popular nonlocal nonlinear media, namely, lead glass. The annular shape and topological charge of the vortex component in the GVVS and GVVB can be preserved during the propagation. The refractive index waveguide induced by the Gaussian component leads to the stabilization of the nonlinear vortex beam when the power ratio exceeds a critical value. These experimental

^{*}zhang041420@126.com[†]dcq424@126.com

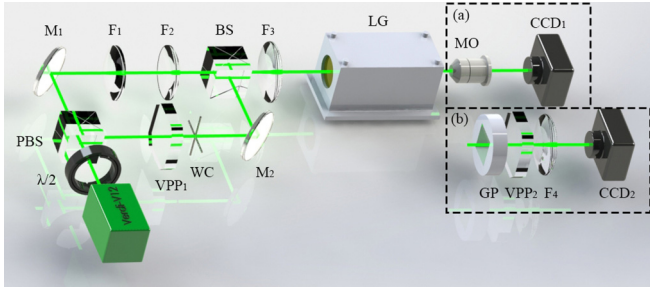


FIG. 1. Sketch of the experimental arrangement. Verdi-V12, Ti-sapphire solid-state green ($\lambda = 532$ nm) laser; $\lambda/2$, half-wave plate; PBS, polarization beam splitter; M_{1-2} , mirrors; VPP_{1-2} , vortex phase plates with charges $l = 10$ and $l = -10$, respectively; WC: wire cross; $F_1 - F_4$, 75, 50, 200, and 150 mm focusing lenses, respectively; BS, beam splitter; LG, lead glass, which is thermally contacted by a copper-made heat sink; MO, $5\times$ microscope objective; GP, Glan prism; CCD_{1-2} , charge-coupled device cameras. Dashed square (a) shows the detecting elements, while dashed square (b) shows the back-converting elements.

results are collaborated by numerical propagations for perturbed stationary solutions of a scalar vortex soliton, GVVS, and GVVb.

II. EXPERIMENTAL SETUP AND RESULTS

A schematic of the experimental arrangement is shown in Fig. 1. The source is a continuous wave (cw) Ti:sapphire solid-state laser with wavelength $\lambda = 532$ nm. The output linearly polarized fundamental beam is split into two components by the polarization beam splitter, PBS. The horizontally polarized Gaussian beam, passing through the telescope composed of F_1 and F_2 , carries the power P_g , whereas the vertically polarized vortex beam, passing through the vortex phase plate VPP_1 , carries the charge $l_v = 10$ and the power P_v . A wire cross, WC, with a diameter of about $150 \mu\text{m}$ is placed behind the VPP_1 , adding initial perturbation corresponding to azimuthal index $k = 4$ to the vortex beam with a diameter of about $w_{p-p} = 5.0$ mm (defined by peak to peak intensity). The two orthogonally polarized beams are combined by the beam splitter, BS, to propagate coaxially, and are focused on the front face of the cylindrical heavily lead-doped glass with length $L = 57.5$ mm and radius $R = 7.5$ mm. The linear refractive index, optical absorption, thermo-optical, and thermal conductivity coefficients of the lead glass are, respectively, $n_0 = 1.9$, $\alpha = 0.07 \text{ cm}^{-1}$, $\beta = 1.4 \times 10^{-5} \text{ K}^{-1}$, and $\kappa = 0.7 \text{ W/(m K)}$ [33]. In dashed square (a), the output scalar and vector beam spots on the rear face of the sample are recorded by the CCD_1 camera (WinCamD-LCM) via a $5\times$ microscope objective, MO. In dashed square (b), the vertically and horizontally polarized components in the composite beam are separated by rotating the Glan prism, GP, and converted to Gaussian spots by passing through VPP_2 with an opposite charge ($l = -10$) and focusing on the CCD_2 camera (WinCamD-UHR).

First, we investigate the linear and nonlinear behaviors of scalar beams propagating alone through the lead glass. As the focal lengths of $F_1 - F_3$ are selected to be 75, 50, and 150 mm,

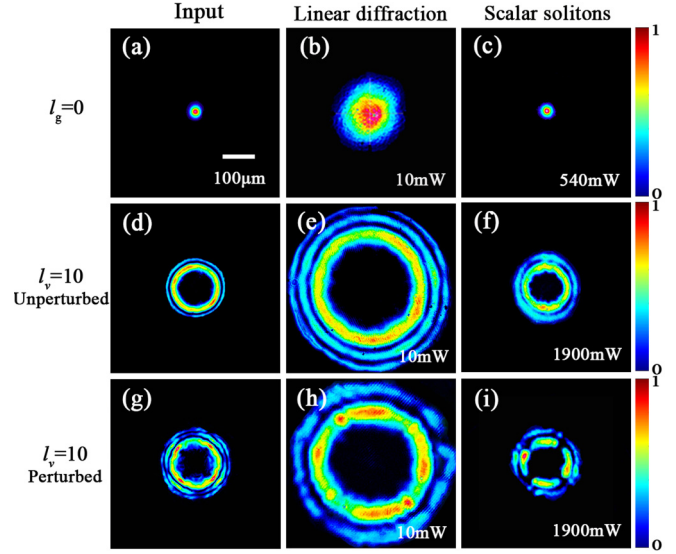


FIG. 2. Experimental beam profiles depicting the linear and non-linear behaviors of scalar beams propagating through a cylindrical lead glass sample. (a)–(c) The scalar Gaussian beam with input beam width $w_{0g} = 19.5 \mu\text{m}$. (d)–(f) The scalar unperturbed vortex beam with input beam width $w_{0v} = 30 \mu\text{m}$. (g)–(i) The scalar vortex beam perturbed by a wire cross.

the input radii for Gaussian beam [Fig. 2(a)] and unperturbed (without wire cross) higher-order vortex [Fig. 2(d)] are $w_{0g} = 19.5 \mu\text{m}$ and $w_{0v} = 30.0 \mu\text{m}$, respectively. Thus, the input beam width ratio of the two components is $\sigma = w_{0g}/w_{0v} = 0.65$, and their normalized diffraction distances are $Z_g = L/k_0 w_{0g}^2 = 6.7$ and $Z_v = L/k_0 w_{0v}^2 = 2.8$, with k_0 being the wave number in media. For low input power of $P_j = 10 \text{ mW}$ ($j = g, v$), both beams diffract without any appreciable non-linear self-action [Figs. 2(b) and 2(e)]. With the increase of input power, these scalar beams undergo self-focusing and shrink gradually, giving rise to a Gaussian soliton [Fig. 2(c)] and a vortex soliton [Fig. 2(f)] at the critical powers of $P_g = 540 \text{ mW}$ and $P_v = 1900 \text{ mW}$, respectively. The observation of a charge-10 vortex soliton without azimuthal breakup is consistent with the results reported earlier [33], where an annulus-preserving charge-4 vortex soliton can be observed just because its normalized diffraction distance was relatively short ($Z_v = 2.1$), and its azimuthal instability has not developed yet. In contrast, by placing a cross filament into the optical setup, the input ring [Fig. 2(g)] is added perturbation corresponding to azimuthal index $k = 4$, and the output vortex clearly splits into four focused fragments under the same input power. This breaking process indicates that perturbation with an appropriate azimuthal index can accelerate the breaking speed upon propagation.

In order to stabilize the perturbed higher-order vortex and prevent its breakup, we investigate the incoherently coupled interaction of two components propagating simultaneously in the form of a GVVS. We have proved that a vector vortex soliton with a given input beam width ratio can exist only at an appropriate power ratio [35]. Thus, for the input Gauss-vortex composite beams with beam width ratio $\sigma = 0.65$ [Figs. 3(a) and 3(c)], we change their power ratio (by rotating the

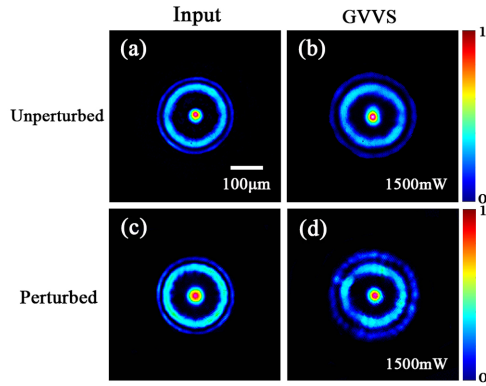


FIG. 3. The formation of the stable GVVS ($l_g = 0$, $l_v = 10$, $\eta = 0.4$) without and with perturbation at the critical power of 1500 mW.

half-wave plate) to a critical value predicted in theory, i.e., $\eta = P_g/P_v = 0.4$, and search for the GVVS by increasing the total input power $P = P_g + P_v$. From the top row in Fig. 3, we can see that the output Gaussian and vortical spots can approach their respective input sizes simultaneously, forming a stable GVVS with a ring shape around a bright center. Obviously, the critical power of the GVVS ($P_c = 1500$ mW) is between those of scalar Gaussian soliton and vortex soliton. In contrast to the beam split in Fig. 2(i), when the perturbed vortex is accompanied by the relatively weak Gaussian beam, its annular shape can be preserved at the soliton power, as shown in Fig. 3(d). It could be said that the azimuthal instability of the higher-order vortex is suppressed due to the cylindrical nonlocal refractive potential induced by the Gaussian soliton.

To confirm the annular shape of the stabilized vortex component, we separately record the constituent components of the output GVVS by rotating the Glan prism placed behind lead glass. The horizontally and vertically polarized components of the perturbed GVVS are displayed in Figs. 4(a) and 4(b), respectively. The comparison of beam profiles in Figs. 2(i) and 4(b) vividly demonstrates the circumvention of vortex breakup and the stabilizing effect of the Gaus-

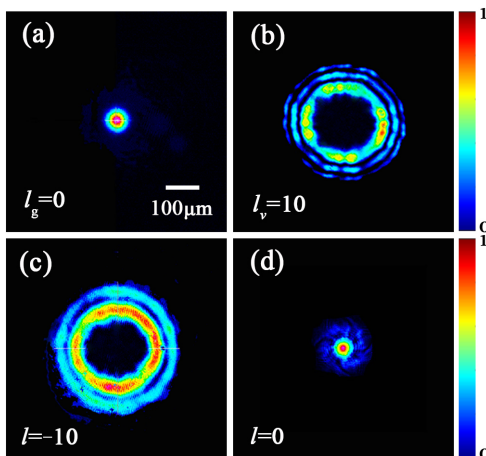


FIG. 4. Beam images of the horizontally (a) and vertically (b) polarized components of the perturbed GVVS displayed in Fig. 3(d). (c,d) Beam images of the horizontally and vertically polarized components passing through VPP₂ with charge $l = -10$, respectively.

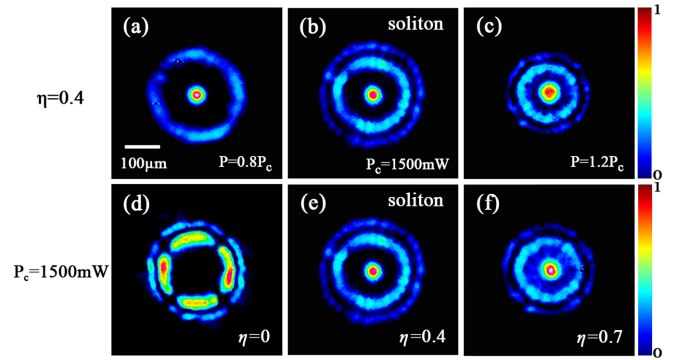


FIG. 5. The output profiles of the GVVB for (a)–(c) various input powers at a fixed power ratio of $\eta = 0.4$ and (d)–(f) various power ratios at a fixed input power of $P_c = 1500$ mW.

sian soliton. On the other hand, the OAM state of a vortex beam can be detected by loading a conjugate spiral phase to eliminate the screw-type phase singularity [36]. As shown in dashed square (b) of Fig. 1, VPP₂ with charge $l = -10$ is used to convert the horizontally polarized Gaussian beam into a vortex beam with charge $l = -10$ [Fig. 4(c)], and convert the vertically polarized vortex beam into a bright fundamental spot [Fig. 4(d)]. This bright spot without phase singularity verifies the preserving of the topological charge of the stabilized vortex. Thus, in summary, we ascertain that the vortex character, including the annular profile and topological charge, of the stabilized vortex is maintained after the propagation.

Finally, we investigate the behaviors of the GVVB when the power of each component deviates from the soliton power. Figures 5(a)–5(c) depict the output spots of the perturbed GVVB with a fixed power ratio of $\eta = 0.4$. As the total power increases, the vortical radius decreases monotonically, whereas the Gaussian radius undergoes aperiodic oscillations. Specifically, the vortical annulus can be preserved in the whole process of increasing power, whenever the input power is less than the critical power or larger than the critical power. On the other hand, at the fixed total power of $P_c = 1500$ mW, we observe the beam profile evolution for various power ratios by rotating the half-wave plate. As shown in Fig. 5(d), the GVVB with $\eta = 0$, i.e., the scalar vortex beam, exhibits a four-lobe azimuthal distortion, which is similar to the breaking scenario in Fig. 2(i). However, when the power ratio $\eta = P_g/P_v$ exceeds the critical power ratio of $\eta = 0.4$, e.g., $\eta = 0.7$ as shown in Fig. 5(f), the annular ring of the perturbed vortex can also be preserved during propagation. Thus, we can conclude that the vortical annulus can be preserved in the GVVB with total power deviating from the soliton power, or in the GVVB with the power ratio exceeding the critical value.

III. NUMERICAL PROPAGATIONS FOR GVVS AND GVVB

To model the experiments presented above, we consider the coaxial propagation of two monochromatic beams with orthogonal polarization in cylindrically symmetric lead glass with strongly thermal nonlocality. Their propagating behaviors

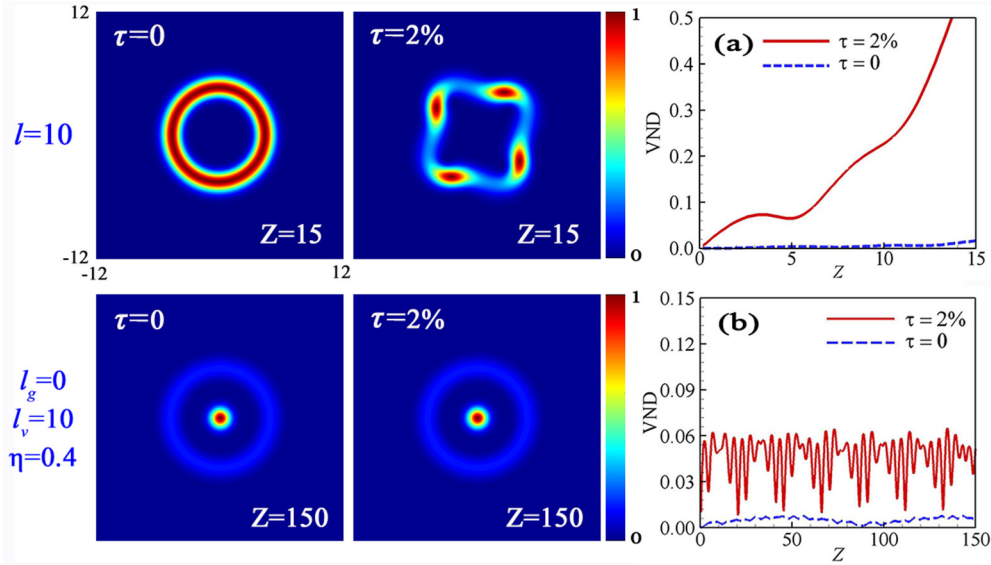


FIG. 6. Top row: the output profiles of the scalar vortex solitons without and with input perturbation, and (a) the growth curves of their VND. Bottom row: the output composite profiles of the GVVS without and with input perturbation, and (b) the growth curves of the VND for vortical components.

can be described by the following coupled equations in cylindrical coordinates (ρ, ϕ, z) [16,33]:

$$2ik_0 \frac{\partial \psi_j}{\partial z} + \left(\frac{\partial^2}{\partial \rho^2} + \frac{1}{\rho} \frac{\partial}{\partial \rho} + \frac{1}{\rho^2} \frac{\partial^2}{\partial \phi^2} \right) \psi_j + 2k_0^2 \frac{\Delta n}{n_0} \psi_j = 0, \quad (1a)$$

$$\left(\frac{\partial^2}{\partial \rho^2} + \frac{1}{\rho} \frac{\partial}{\partial \rho} + \frac{1}{\rho^2} \frac{\partial^2}{\partial \phi^2} \right) \Delta n = -\frac{\alpha\beta}{\kappa} (|\psi_g|^2 + |\psi_v|^2), \quad (1b)$$

where ψ_j is the complex field amplitude, Δn is the nonlinear refractive index, and ϕ is the azimuthal angle. Equation (1) can be simplified to its dimensionless form via the variable and coordinate transformations as follows:

$$q_j = (\alpha\beta k_0^2 r_0^4 / kn_0)^{1/2} \psi_j, \quad n = k_0^2 r_0^2 \Delta n / n_0, \\ r = \rho / r_0, \quad Z = z / k_0 r_0^2, \quad (2)$$

where r_0 is the characteristic beam radius. The dimensionless two-component propagating equations are then

$$i \frac{\partial q_j}{\partial Z} + \frac{1}{2} \left(\frac{\partial^2}{\partial r^2} + \frac{1}{r} \frac{\partial}{\partial r} + \frac{1}{r^2} \frac{\partial^2}{\partial \phi^2} \right) q_j + q_j n = 0, \quad (3a)$$

$$\left(\frac{\partial^2}{\partial r^2} + \frac{1}{r} \frac{\partial}{\partial r} + \frac{1}{r^2} \frac{\partial^2}{\partial \phi^2} \right) n = -(|q_g|^2 + |q_v|^2). \quad (3b)$$

Here, we define the optical power and the statistical beam width as

$$p_j = 2\pi \int_0^\infty r |q_j|^2 dr, \quad w_j = 2\pi \int_0^\infty r^3 |q_j|^2 dr / p_j. \quad (4)$$

The stationary solutions of the scalar vortex soliton and GVVS in the forms of $q_j = \varphi_j(r) \exp(il_j\phi + ib_jZ)$ are sought by Newton's iterative method [33]. We perform numerical

simulations for the scalar vortex soliton and GVVS using the split-step Fourier method. The initial multiplicative perturbation $[1 + \tau \cos(4\phi)]$ is added only into the vortex component, where τ is the perturbation degree. The intrinsic instability of the higher-order vortex will be unveiled during propagation, even though the initial perturbation is random noise. But an appropriate initial perturbation, e.g., $\cos(4\phi)$ in simulation and the one induced by the wire cross in experiment, just accelerates the breaking process of the vortex soliton during propagation. Here, the vector norm deviation (VND) is applied to quantitatively depict the distortion degree of the vortical intensity distribution at any propagation distance $I(Z)$ from the initial one $I(0)$, which is expressed as

$$\text{VND}(Z) = \frac{\|I(Z) - I(0)\|}{\|I(0)\|}. \quad (5)$$

The double bar in Eq. (5) stands for the vector norm, namely, the square root of the sum of squares of each intensity element.

The top row in Fig. 6 shows the dynamical evolutions of the scalar vortex soliton in a lead glass rod with radius $r = 40$. After propagating a relatively short distance of $Z = 15$, the input vortex without perturbation ($\tau = 0$) can temporarily preserve its ring-shaped profile without appreciable deformation (VND = 5%). This dynamics is consistent with that observed in Fig. 2(f), where the azimuthal instability is just in the initial stage of growth. By contrast, a perturbation with $\tau = 2\%$ can quickly lead to vortex decay (VND = 62%) within the same propagation distance, just as that what was experimentally observed in Fig. 2(i). The bottom row in Fig. 6 shows the output composite spots of the GVVS with beam width ratio $\sigma = 0.65$ and power ratio $\eta = 0.4$. Due to the presence of the Gaussian soliton, the higher-order vortex can survive over a considerably longer distance without

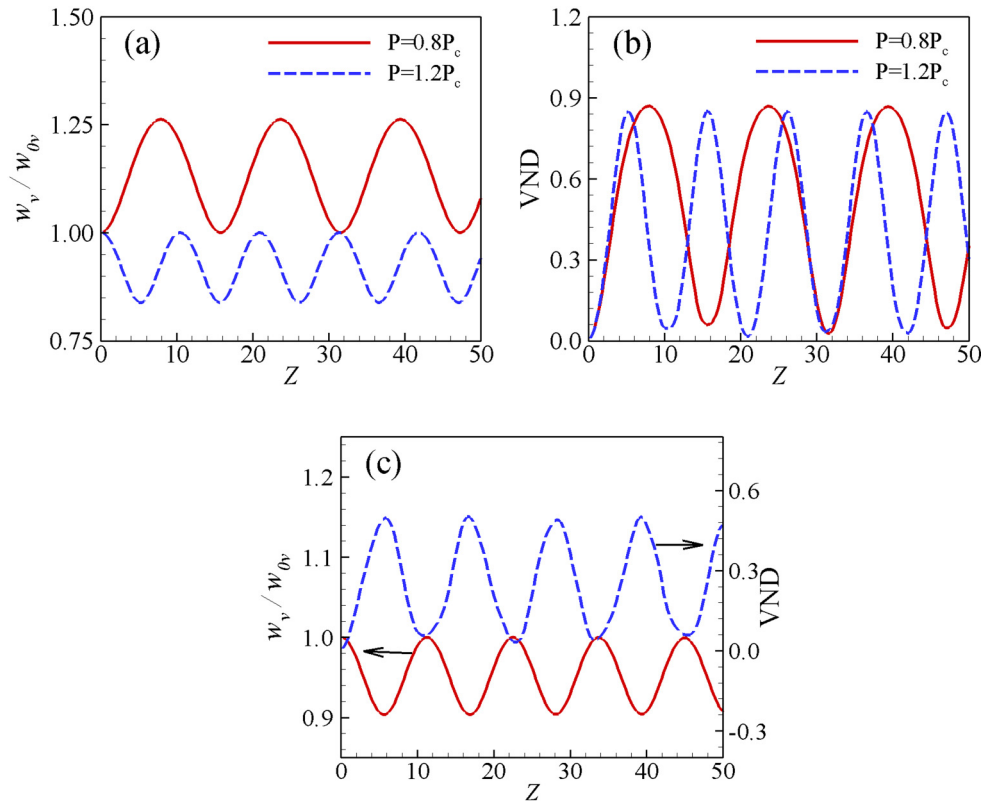


FIG. 7. The vortical beam widths (a) and VND (b) of the perturbed GVVb with $P = 0.8P_c$ and $P = 1.2P_c$. (c) The vortical beam width and VND of the perturbed GVVb with $\sigma = 0.65$ and $\eta = 0.7$.

any azimuthal breakup, whether in the unperturbed case or the perturbed case. It can be seen from Fig. 6(b) that the vortical VND in the unperturbed GVVb approaches zero, while the vortical VND in the perturbed GVVb oscillates within a low level and will not increase during the whole propagation.

Then we investigate the oscillating behaviors of the vortical beam width and VND in the perturbed GVVb. Figure 7(a) shows the normalized vortical beam widths w_v/w_{0v} in the GVVb with $P = 0.8P_c$ and $P = 1.2P_c$. As expected, when the total power is less than the critical power, i.e., $P = 0.8P_c$ shown by the red line, the vortical beam width will first increase and then decrease. On the contrary, when the total power is larger than the critical power, i.e., $P = 1.2P_c$ shown by the dashed blue line, the vortical beam width will first decrease and then increase. As shown in Fig. 7(b), the oscillating frequency of VND is the same as that of the vortical beam width. Specifically, when the vortical beam width oscillates back to its initial size, the VND approaches zero value correspondingly; this case indicates the preserving of the vortical ring profile in the GVVb. Analogous behavior can be seen in Fig. 7(c), where the vortical beam width and VND oscillate synchronously. When the power ratio in the GVVb exceeds the critical value in the GVVb, the vortical annulus in the GVVb can be preserved during the propagation. In fact, such a conclusion was confirmed by performing a lot of numerical propagations for the GVVb with different input beam width ratios.

IV. CONCLUSION

We have experimentally and numerically presented the stabilizing process of the GVVb, formed by one charge-10 vortex soliton copropagating with the other orthogonally polarized Gaussian beam, in thermal nonlocal nonlinear media with a circular cross section. The coupling with the Gaussian soliton circumvents the azimuthal breakup of the charge-10 vortex into four focused fragments that can occur when the perturbed vortex soliton propagates alone. Our experimental results show that the stabilized charge-10 vortex can maintain its vortex characteristics during propagation, i.e., the annular shape and the topological charge. The annular shape of the vortex component in the GVVb can also be preserved during propagation. We expect such a report on a higher-order vortex soliton in lead glass may stimulate further research on more complicated vector solitons, such as higher-order cylindrical-vector solitons and Poincaré solitons with polarization singularities in nonlocal media.

ACKNOWLEDGMENTS

This research was supported by the Scientific Research and Developed Fund of Zhejiang A&F University (Grants No. 2021LFR014 and No. 2021FR0009), the Zhejiang Provincial Natural Science Foundation of China (Grant No. LR20A050001), and the National Natural Science Foundation of China (Grant No.12075210).

- [1] A. M. Yao and M. J. Padgett, Orbital angular momentum: Origins, behavior and applications, *Adv Opt. Photon.* **3**, 161 (2011).
- [2] A. S. Desyatnikov, L. Torner, and Y. S. Kivshar, Optical vortices and vortex solitons, in *Progress in Optics*, edited by E. Wolf (North-Holland, Amsterdam, 2005), Vol. 47, Chap. 5.
- [3] S. Li, X. Pan, Y. Ren, H. Liu, S. Yu, and J. Jing, Deterministic Generation of Orbital-Angular-Momentum Multiplexed Tripartite Entanglement, *Phys. Rev. Lett.* **124**, 083605 (2020).
- [4] W. Wang, K. Zhang, and J. Jing, Large-Scale Quantum Network over 66 Orbital Angular Momentum Optical Modes, *Phys. Rev. Lett.* **125**, 140501 (2020).
- [5] T. Lei, M. Zhang, Y. Li, P. Jia, G. Liu, X. Xu, Z. Li, C. Min, J. Lin, C. Yu, H. Niu, and X. Yuan, Massive individual orbital angular momentum channels for multiplexing enabled by Dammann gratings, *Light Sci. Appl.* **4**, e257 (2015).
- [6] Y. Shen, X. Wang, Z. Xie, C. Min, X. Fu, Q. Liu, M. Gong, and X. Yuan, Optical vortices 30 years on: OAM manipulation from topological charge to multiple singularities, *Light Sci. Appl.* **8**, 90 (2019).
- [7] M. Lavery, F. Speirits, S. Barnett, and M. Padgett, Detection of a spinning object using lights orbital angular momentum, *Science* **341**, 537 (2013).
- [8] P. Gregg, P. Kristensen, and S. Ramachandran, Conservation of orbital angular momentum in aircore optical fibers, *Optica* **2**, 267 (2015).
- [9] M. S. Bigelow, Q. H. Park, and R. W. Boyd, Stabilization of the propagation of spatial solitons, *Phys. Rev. E* **66**, 046631 (2002).
- [10] W. J. Firth and D. V. Skryabin, Optical Solitons Carrying Orbital Angular Momentum, *Phys. Rev. Lett.* **79**, 2450 (1997).
- [11] Y. V. Izdebskaya, A. S. Desyatnikov, G. Assanto, and Y. S. Kivshar, Dipole azimuthons and vortex charge flipping in nematic liquid crystals, *Opt. Express* **19**, 21457 (2011).
- [12] M. S. Bigelow, P. Zerom, and R. W. Boyd, Breakup of Ring Beams Carrying Orbital Angular Momentum in Sodium Vapor, *Phys. Rev. Lett.* **92**, 083902 (2004).
- [13] Z. Chen, M. F. Shih, and M. Segev, Steady-state vortex-screening solitons formed in biased photorefractive media, *Opt. Lett.* **22**, 1751 (1997).
- [14] R. L. Pego and H. A. Warchall, Spectrally stable encapsulated vortices for nonlinear Schrödinger equations, *J. Nonlinear Sci.* **12**, 347394 (2002).
- [15] L. D. Carr and C. W. Clark, Vortices in Attractive Bose-Einstein Condensates in Two Dimensions, *Phys. Rev. Lett.* **97**, 010403 (2006).
- [16] C. Rotschild, O. Cohen, O. Manela, M. Segev, and T. Carmon, Solitons in Nonlinear Media with an Infinite Range of Nonlocality: First Observation of Coherent Elliptic Solitons and of Vortex-Ring Solitons, *Phys. Rev. Lett.* **95**, 213904 (2005).
- [17] Y. V. Izdebskaya, V. G. Shvedov, P. S. Jung, and W. Krolikowski, Stable vortex soliton in nonlocal media with orientational nonlinearity, *Opt. Lett.* **43**, 66 (2018).
- [18] U. A. Laudyn, M. Kwasny, M. A. Karpierz, and G. Assanto, Vortex nematons in planar cells, *Opt. Express* **28**, 8282 (2020).
- [19] Z. Xu, N. F. Smyth, A. A. Minzoni, and Y. S. Kivshar, Vector vortex solitons in nematic liquid crystals, *Opt. Lett.* **34**, 1414 (2009).
- [20] A. A. Minzoni, N. F. Smyth, Z. Xu, and Y. S. Kivshar, Stabilization of vortex-soliton beams in nematic liquid crystals, *Phys. Rev. A* **79**, 063808 (2009).
- [21] Y. V. Izdebskaya, G. Assanto, and W. Krolikowski, Observation of stable-vector vortex solitons, *Opt. Lett.* **40**, 4182 (2015).
- [22] Y. V. Izdebskaya, W. Krolikowski, N. F. Smyth, and G. Assanto, Vortex stabilization by means of spatial solitons in nonlocal media, *J. Opt.* **18**, 054006 (2016).
- [23] M. Shen, J.-J. Zheng, Q. Kong, Y.-Y. Lin, C.-C. Jeng, R.-K. Lee, and W. Krolikowski, Stabilization of counter-rotating vortex pairs in nonlocal media, *Phys. Rev. A* **86**, 013827 (2012).
- [24] Y. V. Izdebskaya, J. Rebling, A. S. Desyatnikov, and Y. S. Kivshar, Observation of vector solitons with hidden vorticity, *Opt. Lett.* **37**, 767 (2012).
- [25] M. Brtko, A. Gammal, and B. A. Malomed, Hidden vorticity in binary Bose-Einstein condensates, *Phys. Rev. A* **82**, 053610 (2010).
- [26] Z. Li, W. Liu, Z. Li, C. Tang, H. Cheng, J. Li, X. Chen, S. Chen, and J. Tian, Tripling the capacity of optical vortices by nonlinear metasurface, *Laser Photon. Rev.* **12**, 1800164 (2018).
- [27] L. Zhu, M. Tang, H. Li, Y. Tai, and X. Li, Optical vortex lattice: An exploitation of orbital angular momentum, *Nanophotonics* **10**, 2487 (2021).
- [28] D. Mihalache, D. Mazilu, L.-C. Crasovan, I. Towers, B. A. Malomed, A. V. Buryak, L. Torner, and F. Lederer, Stable three-dimensional spinning optical solitons supported by competing quadratic and cubic nonlinearities, *Phys. Rev. E* **66**, 016613 (2002).
- [29] T. A. Davydova and A. I. Yakimenko, Stable multi-charged localized optical vortices in cubic-quintic nonlinear media, *J. Opt. A: Pure Appl. Opt.* **6**, S197S201 (2004).
- [30] Y. Li, Z. Chen, Z. Luo, C. Huang, H. Tan, W. Pang, and B. A. Malomed, Two-dimensional vortex quantum droplets, *Phys. Rev. A* **98**, 063602 (2018).
- [31] J. Qin, G. Dong, and B. A. Malomed, Stable giant vortex annuli in microwave-coupled atomic condensates, *Phys. Rev. A* **94**, 053611 (2016).
- [32] B. A. Malomed, Vortex solitons: Old results and new perspectives, *Phys. D (Amsterdam, Neth.)* **399**, 108 (2019).
- [33] H. Zhang, M. Chen, L. Yang, B. Tian, C. Chen, Q. Guo, Q. Shou, and W. Hu, Higher-charge vortex solitons and vector vortex solitons in strongly nonlocal media, *Opt. Lett.* **44**, 3098 (2019).
- [34] H. Zhang, Z. Weng, Q. Shou, Q. Guo, and W. Hu, Instability suppression of vector vortex solitons in nonlocal nonlinear media, *Phys. Rev. A* **101**, 033842 (2020).
- [35] H. Zhang, Z. Weng, and J. Yuan, Vector vortex breathers in thermal nonlocal media, *Opt. Commun.* **492**, 126978 (2021).
- [36] J. Yu, C. Miao, J. Wu, and C. Zhou, Circular Dammann gratings for enhanced control of the ring profile of perfect optical vortices, *Photon. Res.* **8**, 648 (2020).